# Band gap opening in the BiSbTeSe$_2$ topological surface state induced by ferromagnetic surface reordering

A. K. Kaveev [1,*] S. M. Suturin [1] V. A. Golyashov,[2] K. A. Kokh,[3] S. V. Eremeev,[4,5] D. A. Estyunin [6] A. M. Shikin,[6]
A. V. Okotrub,[7] A. N. Lavrov [7] E. F. Schwier [8] and O. E. Tereshchenko[2,9]

[1]*Solid state physics department, Ioffe Institute, 194021 Saint-Petersburg, Russia*
[2]*Rzhanov Institute of Semiconductor Physics, 630090 Novosibirsk, Russia*
[3]*Sobolev Institute of Geology and Mineralogy, 630090 Novosibirsk, Russia*
[4]*Institute of Strength Physics and Materials Science, 634055 Tomsk, Russia*
[5]*Tomsk State University, 634050 Tomsk, Russia*
[6]*Saint-Petersburg State University, 198504, Saint-Petersburg, Russia*
[7]*Nikolaev Institute of Inorganic Chemistry, SB RAS, 630090 Novosibirsk, Russia*
[8]*Julius-Maximilians University, D-97074 Würzburg, Germany*
[9]*Novosibirsk State University, 630090 Novosibirsk, Russia*

Introducing magnetic exchange interaction into topological insulators is known to break the time-reversal symmetry and to open a gap at the Dirac point in the otherwise gapless topological surface states. This allows various novel topological quantum phenomena to be attained, including the quantum anomalous Hall effect and can lead to the emergence of the axion insulator phase. Among the different approaches, magnetic doping is an effective, but still experimentally challenging pathway to provide the magnetic exchange interaction. Here we demonstrate that epitaxial deposition of Co and Mn magnetic atoms onto the (0001) surface of the BiSbTeSe$_2$ topological insulator with a coverage between 0.6 and 3 atoms per surface cell performed in a finely tuned temperature range of 300°–330°C leads to the substitution of pnictogen atoms in the surface layer with magnetic atoms and to the formation of a two-dimensional magnetic phase with out-of-plane magnetization as proved by SQUID magnetometry. This magnetic layer is responsible for the appearance of a gap in the Dirac surface state as revealed by laser-based microfocused angle-resolved photoelectron spectroscopy. Our measurements have shown that the gap exists within the temperature range of 15–100 K, where the out-of-plane magnetization persists. The presented experimental results are supported by relativistic *ab initio* calculations.

## I. INTRODUCTION

Topological insulators (TIs) are a kind of novel quantum materials which are characterized by the unique bulk band structure, where owing to a strong spin-orbit interaction (SOI) the bulk conduction and bulk valence band parities are inverted at a certain point in the Brillouin zone. This band inversion gives rise to a spin-momentum locked gapless metallic state with Dirac dispersion appearing at the surface of the material, which is protected by time reversal symmetry (TRS) [1,2]. By breaking TRS, e.g., via ferromagnetism, the Dirac energy dispersion acquires a gap. This gap is required for realization of many novel quantum effects, such as the quantum anomalous Hall effect (QAHE), which manifests as the dissipationless chiral edge states in the absence of an external magnetic field, topological magnetoelectric (TME) effects, and chiral Majorana modes [3–5].

Several approaches can be implemented to introduce magnetic exchange interaction in TIs. Apart from growth of intrinsic magnetic topological insulators [6] it can be achieved via magnetic atom doping [7], which allowed one to realize the QAHE for the first time in Cr$_{0.15}$(Bi$_{0.1}$Sb$_{0.9}$)$_{1.85}$Te$_3$ [8]. Following the experimental discovery of the QAHE by Chang *et al.* it has been observed and reported for the molecular-beam-epitaxy (MBE) grown (Bi, Sb)$_2$Te$_3$ thin films doped with magnetic elements such as Cr and V [9–18]. The incorporation of Mn atoms into the TIs was revealed to occur in different ways, depending on experimental conditions: It can result in the formation of dilute magnetic alloys (Mn$_x$A$_{1-x}$)$_2$B$_3$ (where $A$ = Bi,Sb and $B$ = Se,Te) [19–25] as well as in formation of septuple layers (SL). The latter can occur during MBE epitaxial growth of bulk crystals when the beams of Bi(Sb), Se(Te), and Mn atoms are incident onto the surface resulting in the formation of self-assembled layers of MnBi(Sb)$_2$Se(Te)$_4$ which randomly intersperse between quintuple layers (QLs) of pure $A_2B_3$ ($A$ = Bi,Sb and $B$ = Se,Te) [26,27]. In particular for MnBi$_2$Te$_4$-Bi$_2$Te$_3$ random heterostructures, low-temperature photoelectron spectroscopy measurements allowed revealing the magnetic gap of up to 90 meV [27]. It was also shown in [28] that such structure may act as "half-magnetic topological insulator" with the magnetization existing at the MnBi$_2$Te$_4$ surface but not at the opposite surface terminated by triple Bi$_2$Te$_3$ layers.

*kaveev@mail.ioffe.ru

Earlier, a similar gap (of ∼100 meV) was achieved in the $MnBi_2Se_4/Bi_2Se_3$ two-dimensional (2D) heterostructure prepared by codepositing Mn and Se on top of the $Bi_2Se_3$ surface, in which case a single $MnBi_2Se_4$ SL was formed [29]. Several 2D heterostructures composed of TI with a magnetic block on top were also predicted theoretically [30,31]. The $MnBi_2Te_4/Bi_2Te_3$ 2D heterostructure along with a more complicated $Mn_4Bi_2Te_7/Bi_2Te_3$ was realized recently [32]. In contrast to this, surface deposition of magnetic Fe and Co atoms demonstrates a lot of controversy. Earlier reports on Fe deposition at $Bi_2Se_3$ manifested a gap at the Dirac point [33]. However, latter experiments on Fe and Co deposition did not reveal the gap opening and x-ray magnetic circular dichroism (XMCD) measurements have shown absence of ferromagnetic ordering [34–37]. At the same time it was shown by x-ray absorption fine structure (XAFS) measurements that annealing of iron deposited at the $Bi_2Se_3$ surface up to 520 K can lead to the formation of the $\alpha$-FeSe phase [38]. The surface band gap of ∼100 meV was observed in epitaxial $(Bi_{1-x}Mn_x)_2Se_3$. However, it was shown that this gap is neither due to ferromagnetic order in the bulk or at the surface nor to the local magnetic moment of the Mn. It was demonstrated using resonant photoemission that resonance states present in the bulk gap and suggested that the gap at the Dirac point is caused by strong resonant scattering processes [39]. On the other hand, angle-resolved photoelectron spectroscopy measurements on V-doped $(Bi, Sb)_2Te_3$ do not reveal the gap at the Dirac point down to 1 K [40]. The observed controversy is related to deposition conditions such as coverage, deposition temperature, and post-growth annealing.

In the present work, we report on the successful experimental manifestation of the gapped Dirac state in $BiSbTeSe_2$ (hereinafter BSTS2) TI with a precisely magnetically doped surface layer. In contrast to the prototype three-dimensional TIs, such as $Bi_2Se_3$ and $Bi_2Te_3$, which have a significant bulk conductance due to the intrinsic defects and the resulting unintentional bulk doping, $BiSbTeSe_2$ exhibits a surface-dominated conductivity [41,42]. We show that in the range of surface coverage of 0.6–3 atoms/cell, deposition of cobalt performed at 300°–330°C, results in formation of ferromagnetic surface QL with Co substitution for Bi and emergence of a gap of 21 ± 6 meV in the surface Dirac spectrum. Increasing the Co coverage leads to formation of islands of paramagnetic orthorhombic $CoTe_xSe_{2-x}$ phase. Similar results were obtained for Mn deposition, where the gap in the Dirac state was found to be 37 ± 9 meV.

## II. METHODS

BSTS2 monocrystalline substrates were made from BSTS2 bulk monocrystals, which were grown by the modified vertical Bridgeman method from the previously synthesized mixture of 5N pure Bi, Sb, Te, and Se.

Clean TI surfaces were obtained by the cleaving with a scotch tape and a subsequent vacuum annealing at 330 °C during 30 min under $10^{-8}$ mBar pressure. Co and Mn were deposited from a conventional e-beam source, and Co was also deposited with the use of the laser molecular beam epitaxy (MBE) system (produced by Surface, GmbH) based on a KrF

excimer laser. Both materials were deposited on BSTS2 at temperatures ranging from room temperature (RT) to 330 °C.

The amounts of Co and Mn coverage were estimated from flux calibration carried out by a quartz thickness monitor and expressed as the number of adsorbate atoms per the 4.4 Å × 4.4 Å rhombic surface unit cell of BSTS2. This coverage was up to 3 Co atoms and 1.36 Mn atoms per unit cell. Additional experiments with a Co coverage of 135 atoms per unit cell were also carried out.

The electronic structure of the grown samples was studied by laser-based microfocused angle-resolved photoelectron spectroscopy (laser-$\mu$ARPES) at a 13- to 150-K temperature range. The laser-$\mu$ARPES method is a powerful tool for studying the electronic band dispersion in general and fine features of the surface band structure like gapped Dirac cones. To select the direction in the $k$ space used for laser ARPES studies, Lauegrams of each sample were measured and used for the sample orientation along high symmetry directions. To identify the precise $\Gamma$-point position, reciprocal space ($k_x$, $k_y$) mapping around the $\Gamma$ point was carried out. The sample surface composition was studied by the x-ray photoelectron spectroscopy (XPS) using an SPECS photoelectron spectrometer with a PHOIBOS 150 MCD 9 hemispherical analyzer and a FOCUS 500 x-ray monochromator (AlK$\alpha$ emission line, $h\nu$ = 1486.74 eV). The binding energy scale was calibrated using the Au $4f_{7/2}$ (84.0 eV) core level position. The Co/BSTS2 surface morphology was studied using atomic force microscopy (microscope produced by NT-MDT).

Magnetization measurements were carried out using a Quantum Design MPMS-XL SQUID magnetometer at fields up to 1 T applied along one of the crystal axes. The data were collected upon sweeping the temperature in the range 1.8–250 K, with averaging the records from several cooling-heating runs to reduce the data dispersion. By subtracting the value of magnetization measured at $T$=250 K, $M_{250K}$, from the $M(T)$ curve we could therefore get rid of all extrinsic contributions together with the predominant intrinsic diamagnetic contribution of the BSTS2 crystal and emphasize the magnetization features emerging at low temperatures.

Density functional theory calculations were performed by using the Vienna *Ab initio* Simulation Package (VASP) [43,44], with core electrons represented by projector augmented wave (PAW) potentials [45,46]. We used generalized gradient approximation (GGA-PBE) [47] to describe the exchange-correlation potential. DFT-D3 van-der-Walls correction method with Becke-Johnson damping [48] was applied for accurate structure optimization of the doped topological insulators. For calculation of the total energy of CoTeSe in ferromagnetic and paramagnetic phases we applied the special quasirandom structures (SQS) approach [49] to construct a 2 × 2 × 2 supercell using the SUPERCELL program [50] to randomize Te and Se atoms on chalcogen sublattice as well as Co magnetic moments in the paramagnetic phase.

## III. RESULTS

### A. Band gap opening in the BSTS2 induced by the Co deposition

The BSTS2 (0001) surface was prepared by the cleavage in ultrahigh vacuum (∼$10^{-10}$ mbar). The laser-ARPES
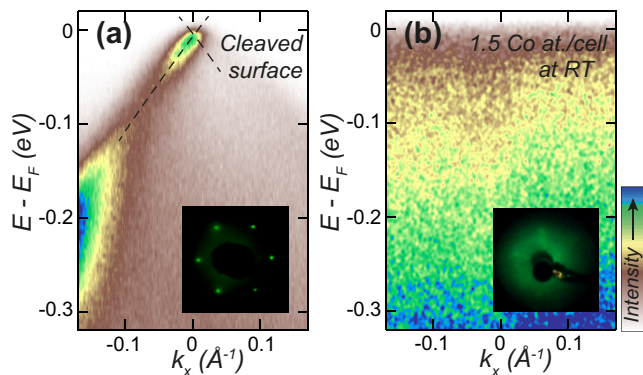
FIG. 1. Laser-ARPES spectra measured at 13 K of a clean cleaved BSTS2 surface (a) and a BSTS2 surface with 1.5 Co atoms per BSTS2 unit cell deposited at room temperature (b). The inserts in the figures show corresponding LEED patterns.

dispersion map of the fresh BSTS2 surface demonstrates the presence of a holelike state with a quasilinear dispersion at the Fermi level [Fig. 1(a)]. This surface is characterized by the $(1 \times 1)$ LEED pattern [insert in Fig. 1(a)]. The linear-dispersing state can be easily identified as the topological surface state (TSS) with the Dirac point being present at the Fermi level. Under such conditions, the observation of any changes in the electronic structure of the TSS near the Dirac point by ARPES would be complicated. In contrast, Fig. 1(b) demonstrates the laser-ARPES map measured for the BSTS2 surface with a large amount of Co deposited at room temperature which will be discussed further.

Deposition of an ultrasmall amount of Co atoms (about 0.1–0.2 atoms per surface cell of BSTS2) at room temperature leads to the downward band bending (electron doping) making the Dirac point easily accessible [Fig. 2(a)]. Figures 2(b) and 2(c) show zoomed images of the spectrum and its second derivative, respectively. Further Co deposition at room temperature leads to progressive surface disordering and at coverage of 1.5 Co atoms per cell to complete disappearance of band dispersion in the laser-ARPES map [Fig. 1(b)] and to degradation of the LEED pattern [insert in Fig. 1(b)]. Unlike previous studies reporting on retention of the ARPES band dispersion at similar magnetic adsorbate coverage deposited at room temperature [36,51–53], the disappearance of band dispersion in our laser-ARPES experiment apparently can be explained by much lower photon energy and consequently, much lower photoemitted electron kinetic energy (1–2 eV) in the laser-ARPES as compared with synchrotron or gas discharge lamp-based ARPES, which leads to higher sensitivity of this technique to large work function variations across the sample surface.

In contrast to the low temperature experiment, Co deposition in the temperature range of 300°–330°C retains the surface ordering up to 3 Co atom/cell and as a result the band structure is clearly visible in the ARPES spectra [Figs. 2(d)–2(h)]. Starting from the coverage of 0.6 atom/cell the TSS exhibits a gap in the Dirac point. Figures 2(e) and 2(f) show zoomed images of the spectrum at 0.6 Co atom/cell and its second derivative, respectively. The gap size for the coverage of 0.6 atom/cell is deduced from the energy distribution

curves (EDCs). For accurate determination of the gap we have selected several EDCs at different $k_{\parallel}$ [Fig. 2(i)]. The data in Fig. 2(i) were fitted using two Voigt profiles for the lower and upper Dirac cone states and a Shirley-type background. The third Voigt profile was added to account for the asymmetry of the upper Dirac cone. The third peak shows a clear electron-like dispersion and can indicate formation of a new crystalline phase at the BSTS2 surface. The derived energy positions of the fitted peaks for different $k_{\parallel}$ are shown in Figs. 2(e) and 2(f). The fitted gap width at the $\bar{\Gamma}$ point for 0.6 atom/cell coverage was defined as $21 \pm 6$ meV.

The dependence of the gap size on the amount of deposited cobalt is shown in Fig. 2(j). It was found to be constant within the measurement error and not dependent on the amount of deposited cobalt at low coverages between 0.6–1.5 at./cell. Despite broadening of the EDC peaks and reducing signal-to-noise ratio of the spectra for Co deposition of 3 at./cell, we have estimated the gap in this case as 37 meV. This value is considerably larger than that at lower coverage. Besides, in this case the band structure is shifted towards the Fermi level as compared to lower coverage. Both factors can indicate additional changes in surface conditions at 3 at./cell coverage. Unfortunately, the gap cannot be resolved at the higher Co amount and its further behavior with increasing Co coverages was inaccessible to the ARPES. Our measurements have shown that the gap width is weakly temperature dependent in the range of 13–150 K (see Fig. S1 in Supplemental Material [54]). At similar deposition conditions we have observed an analogous band bending and a gap opening upon submonolayer deposition of Mn [54].

To better understand how the deposited cobalt modifies the BSTS2 surface we have performed an atomic force microscopy (AFM) study of the surface morphology at different cobalt coverages. The AFM image of a clean BSTS2 surface is shown in Fig. 3(a) while the surface morphologies resulting from effective Co coverage of 1.2, 3, and 135 Co atoms per BSTS2 unit cell are shown in Figs. 3(b), 3(c) and 3(d), respectively. At the early deposition stage, islands with a lateral size of about 30–40 nm and a height of a few nm grow on the BSTS2 surface. These islands get progressively larger as more Co is deposited. At a coverage of 135 Co atoms per unit cell a system of three-dimensional long stripes oriented at 120° to each other is formed at the surface. The crystal structure of the adsorbate layer can be extracted from the RHEED patterns taken in the [010] azimuth and shown in the insets in Fig. 3. As the amount of deposited cobalt is increased, the initially streaky pattern of the clean BSTS2 surface gets gradually replaced by the pattern of the adsorbate layer characterized by a slightly larger interstreak distance. The streaks of the substrate and the overlayer can be seen simultaneously at the coverage of 3 Co atoms per unit cell while at a much higher coverage of 135 Co atoms per unit cell the intensity modulations appear along the streaks allowing identification of the crystal structure of the adsorbate layer. The lattice parameters of this layer were calculated using the absolute RHEED map scale derived from the earlier measured BSTS patterns for which the lattice constants are exactly known.

The rather complicated RHEED pattern was deciphered using the three-dimensional (3D) mapping RHEED analysis technique [55]. This method allows obtaining three-
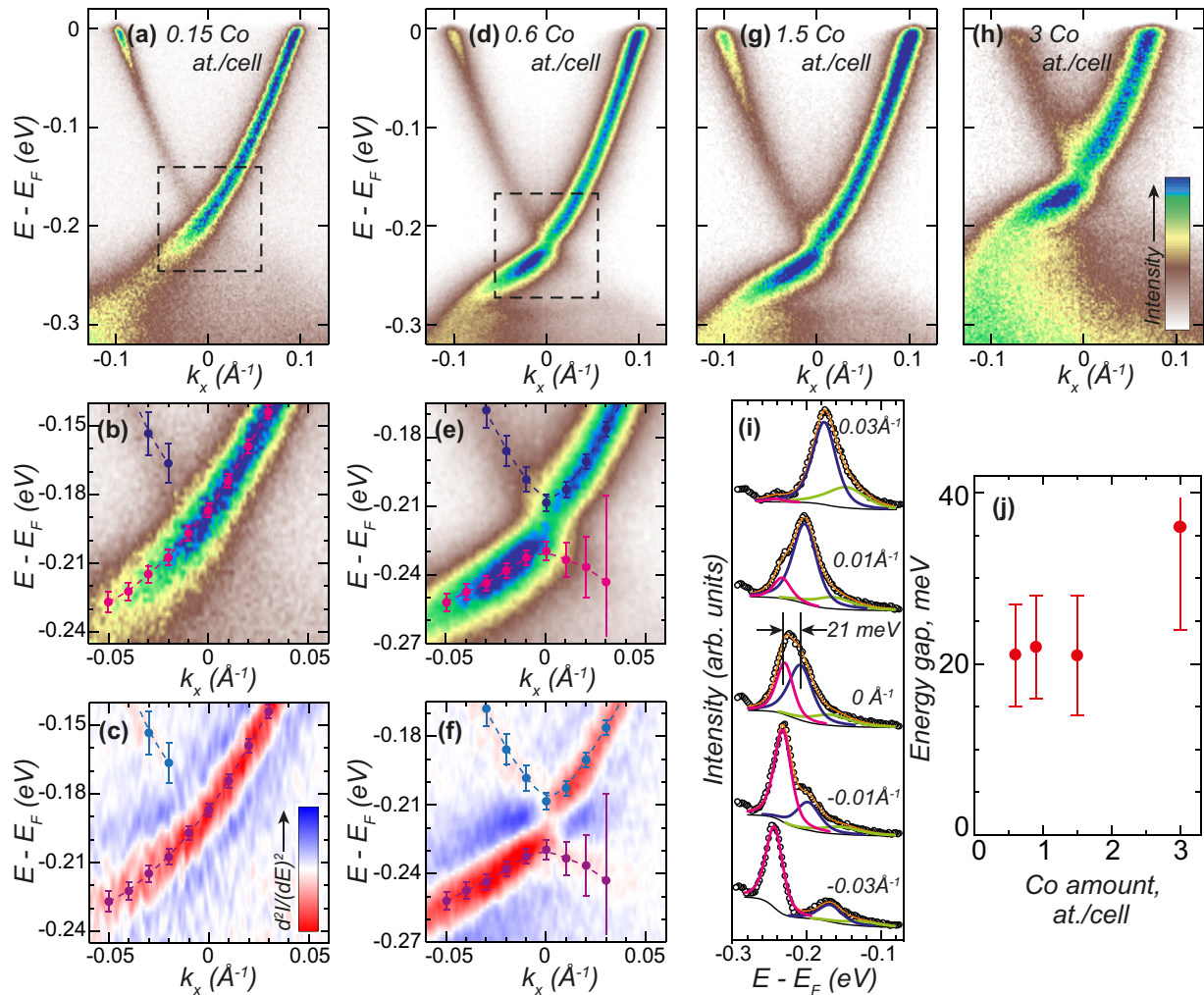
FIG. 2. Laser-ARPES studies of the Co-BSTS2 system near the Dirac point at 13 K. Changes in electronic structure of the BSTS2 surface resulting from deposition of 0.15 (a), 0.6 (d), 1.5 (g), and 3 (h) Co atoms per BSTS2 unit cell at the substrate temperature of 300°C. Appearance of the energy gap at the Dirac point can be clearly seen in spectra (d)–(h). Regions of the ARPES spectra of BSTS2 topological surface states near the Dirac point (Γ-K direction) for samples with a coverage of 0.15 (b) and 0.6 (e) Co atoms per BSTS2 unit cell with their second derivatives $d^2I/dE^2$ (c) and (f), respectively. (i) EDC intensity profiles for different $k_\parallel$ values of the spectrum (d) in this figure (0.6 Co atoms per unit cell). The data were fitted using two Voigt profiles for the lower (red curve) and the upper (blue curve) Dirac cone states, and a Shirley background; the third Voigt profile (green curve) was used to account for the asymmetric lower binding energy tail of the spectral weight. The derived energy positions of the fitted peaks are plotted as points and dashed lines in (e) and (f). (j) The gap width dependence on the amount of cobalt deposited.

dimensional reciprocal space maps from a sequence of diffraction patterns taken during a fine-step rotation of the sample. The obtained 3D maps consisting of dense stacks of Ewald spherical sections can be conveniently analyzed by performing planar cuts perpendicular to the chosen crystallographic axes. Looking at the reciprocal space plan view projection [viewed along the surface normal, see details for further discussion in Fig. 3(e)], one can notice three sets of primitive rectangular lattices. The size of the corresponding direct space unit cell can be estimated as 5.86 Å and 3.66 Å. The three sets are rotated by 120° with respect to each other around the surface normal in full accordance with the $C_3$ symmetry of the substrate surface. The side cuts of the reciprocal space can be fit with a rectangular net of nodes with an out-of-plane distance of 4.99 Å. The H0L plane exhibits systematic absences of type H + K = 2n (n – integer), corresponding to

the presence of a glide plane. With known unit cell parameters and a good match of reciprocal space nodes, including the systematic absence of several nodes, it becomes possible to identify the crystal structure with a sufficient accuracy. The two closest matches with a space group No. 58 *Pmnn* are CoSe$_2$ (4.896 Å, 5.821 Å, 3.643 Å) and CoTe$_2$ (5.301 Å, 6.298 Å, 3.882 Å). With the former lattice being slightly smaller and the latter one slightly larger than the one observed, we assume that the layer formed due to cobalt deposition has a mattagamite-type CoTe$_x$Se$_{2-x}$ structure. The revealed epitaxial relations are [100] CoTe$_x$Se$_{2-x}$ ∥ [001] BSTS2; [001] CoTe$_x$Se$_{2-x}$ ∥ ⟨0$\bar{1}$0⟩ BSTS2. Our finding is in agreement with the earlier observation of CoTe$_2$ (CoSe$_2$) compounds forming upon Co deposition on Bi$_2$(Te, or Se)$_3$ in Ref. [56].

A rough estimation shows that a cobalt coverage of 1.2 atoms per BSTS2 unit cell is sufficient to build a 4.6-Å uni-
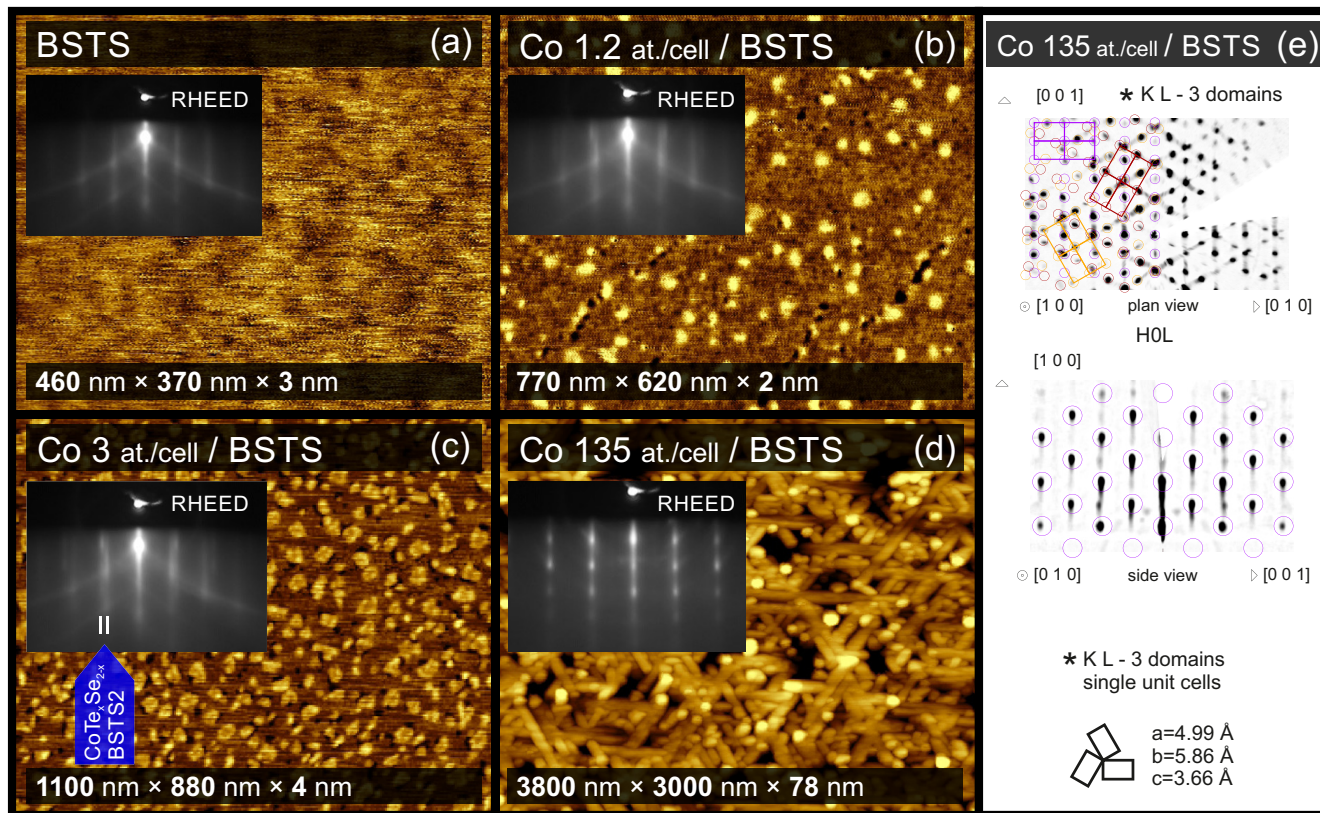
FIG. 3. Evolution of the BSTS2 surface morphology upon Co deposition. AFM image of a clean BSTS2 surface (a), and the same surface with an effective cobalt coverage of 1.2 (b), 3 (c), and 135 (d) Co atoms per BSTS2 unit cell. Shown in the insets are the corresponding RHEED patterns taken in the [010] azimuth. Plan and side view reciprocal space projections obtained by RHEED are shown in panels (e) top, and (e) bottom with the superimposed model of mattagamite reciprocal lattice (three rotational domains at 120° to each other).

form layer of mattagamite or to cover 20% of the surface with islands of 23 Å in height. The latter configuration is very similar to that shown in Fig. 3(b). This allows us to suppose that most of the deposited cobalt atoms spent on the formation of CoTe$_x$Se$_{2-x}$ islands, while a smaller amount of cobalt atoms remains diluted within the BSTS2 surface layer.

Comparing AFM, RHEED, and ARPES data we assume that an almost uniform layer is formed on the BSTS2 surface at or below cobalt coverage of 0.6 atoms per BSTS2 unit cell opening the gap in the band structure. Simultaneously or just after Co dilution in the QL fully completes, the mattagamite islands nucleate on top, masking the modified BSTS2 surface, which results in broadening of ARPES spectra but does not affect the gap.

### B. Electronic structure calculations for Co-doped TIs

To shed light on the effect of deposited Co on the electronic structure of the BSTS2 topological insulator we performed density functional theory (DFT) calculations. In contrast to the prototypical topological insulators such as Bi$_2$Te$_3$, Bi$_2$Se$_3$, and Sb$_2$Te$_3$ which are intrinsically $n$- or $p$-doped insulators showing metallic bulk conductivity, BiSbTeSe$_2$ is a compensated insulator due to suppression of the defect-induced charge density by mixing of Bi with Sb, and Te with Se in pnictogen and chalcogen sublattices, respectively. However, as far as the defect-induced doping is absent in DFT

calculations we have considered the substitutional Co atoms incorporated into Bi(Sb) sites in three parent binary compounds. As the initial guess for the structure of the Co submonolayer coverage, we assume that pnictogen atoms in the top layer of the BSTS2 substrate are partially substituted by cobalt. At a higher coverage this naturally serves as a precursor for the nucleation of the orthorhombic mattagamitelike phase observed by RHEED. For this reason we have chosen a $\sqrt{3} \times 2$ rectangular surface cell containing four atoms in each atomic layer. Within this cell one of the four pnictogen atoms in the second atomic layer is replaced by a Co atom [see Figs. 4(a) and 4(b)]. It should be noted, that the calculated Co magnetic moments have preferable out-of-plane spin orientation that is energetically favorable with respect to their in-plane alignment for all considered systems. The magnetic moments were found to be the same, 2.46 $\mu_B$, for Co in Bi$_2$Te$_3$ and Sb$_2$Te$_3$, while it is a bit larger for Bi$_2$Se$_3$, being equal to 2.56 $\mu_B$. The spectra of $\sqrt{3} \times 2$ slabs of Bi$_2$Te$_3$, Bi$_2$Se$_3$, and Sb$_2$Te$_3$ are presented in Figs. 4(c)–4(e). All spectra show a gap in the Dirac state that equals to 14 and 12 meV for Bi$_2$Te$_3$ and Bi$_2$Se$_3$, respectively, while it is noticeably larger, 43.5 meV, for Sb$_2$Te$_3$. However, decreasing Co concentration in the Sb layer of Sb$_2$Te$_3$ by constructing larger surface cells to 1/6 ($\sqrt{3} \times 3$) and to 1/12 ($2\sqrt{3} \times 3$) leads to an almost linear decrease in the gap [Fig. 4(f)]. In general, the gap width in the parent binary TIs with a moderate Co substitution is in good agreement with the experimental gap of 21 ± 6 meV in
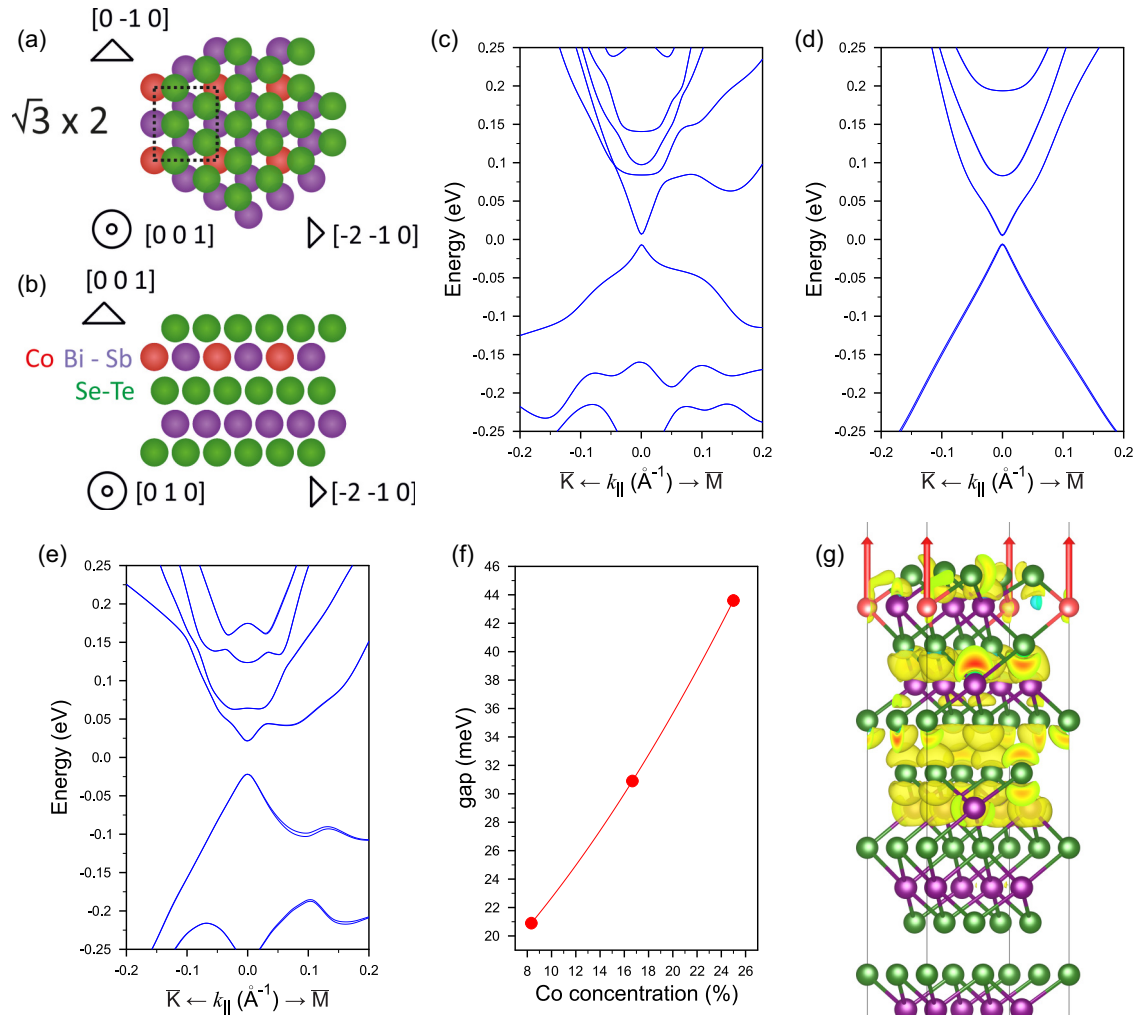
FIG. 4. Calculated electronic structure of the topological insulator doped with Co. Schematic atomic structure of the $\sqrt{3} \times 2$ surface cell where second layer pnictogen atoms partially substituted with cobalt: top (a) and side (b) view. Surface spectrum for the slab with a concentration of Co in the first pnictogen layer of 25% in $Bi_2Te_3$ (c), $Bi_2Se_3$ (d), and $Sb_2Te_3$ (e). (f) Gap width in Co-doped $Sb_2Te_3$ as a function of Co concentration. (g) Spatial charge distribution of the gapped topological surface state. Red arrows show Co magnetic moments.

the Co-doped $BiSbTeSe_2$. Similar to the gapless Dirac state in $Bi_2Te_3$-type TIs the gapped state in the case of Co substitution is localized mainly within outer QL and near the first van-der-Waals spacing [Fig. 4(g)], where it overlaps with orbitals of substitutional Co atoms.

## C. Magnetization measurements after Co deposition

Magnetization measurements of the BSTS crystal with deposited cobalt performed for the field orientation $H \perp c$ (in-plane) have revealed a considerable nonlinear magnetization (field-dependent susceptibility $\chi = M/H$) that shows up below 70–80 K. To emphasize this peculiar feature and to get rid of both the extrinsic susceptibility contribution and the intrinsic diamagnetic one, $\chi_{DM}$, that dominates the magnetic response ($\chi_{DM} \sim (3.3 - 4.8) \times 10^{-7}$ emu/g), we subtracted the susceptibility values at $T = 250$ K and plotted the product $\chi - \chi_{250K}$ as a function of temperature and magnetic field [Fig. 5(a)]. The resulting susceptibility apparently contains two contributions: a paramagnetic (PM) one that is weakly dependent on magnetic field and becomes considerable at

temperatures below $\sim$10 K, and a ferromagnetic (FM) one that emerges below $T \sim$80–100 K and is best seen at weak magnetic fields. By plotting the $M(H)$ data at a temperature where the FM contribution is already fully developed while the PM one is still subtle, one can determine both the FM magnetization contribution and the field where the FM moment saturates [inset in Fig. 5(a)]. As can be seen, the saturation field is rather small, $\sim$500 Oe, confirming that a long-range FM order is formed. The evaluated FM moment is $\approx 2 \times 10^{-6}$ emu, which corresponds to $\approx 2.4 \times 10^{14}$ $\mu_B/cm^2$ ($\approx 2.4$ $\mu_B/nm^2$) given the crystal surface $\approx 0.9$ cm$^2$. This estimation has a reasonable agreement with the density of magnetic Co ions in the surface layer. Similar measurements and data analyzes performed for another orientation of the crystal with respect to the magnetic field, $H \| c$ (out-of-plane), revealed a smaller FM magnetization contribution [Fig. 5(b)] in comparison with the in-plane magnetization. The observed anisotropy gives a strong evidence in favor of the intrinsic origin of the revealed FM moment. One can suggest that the magnetization easy axis of a built-in Co layer is outside the plane and there is a projection of the magnetization vector on
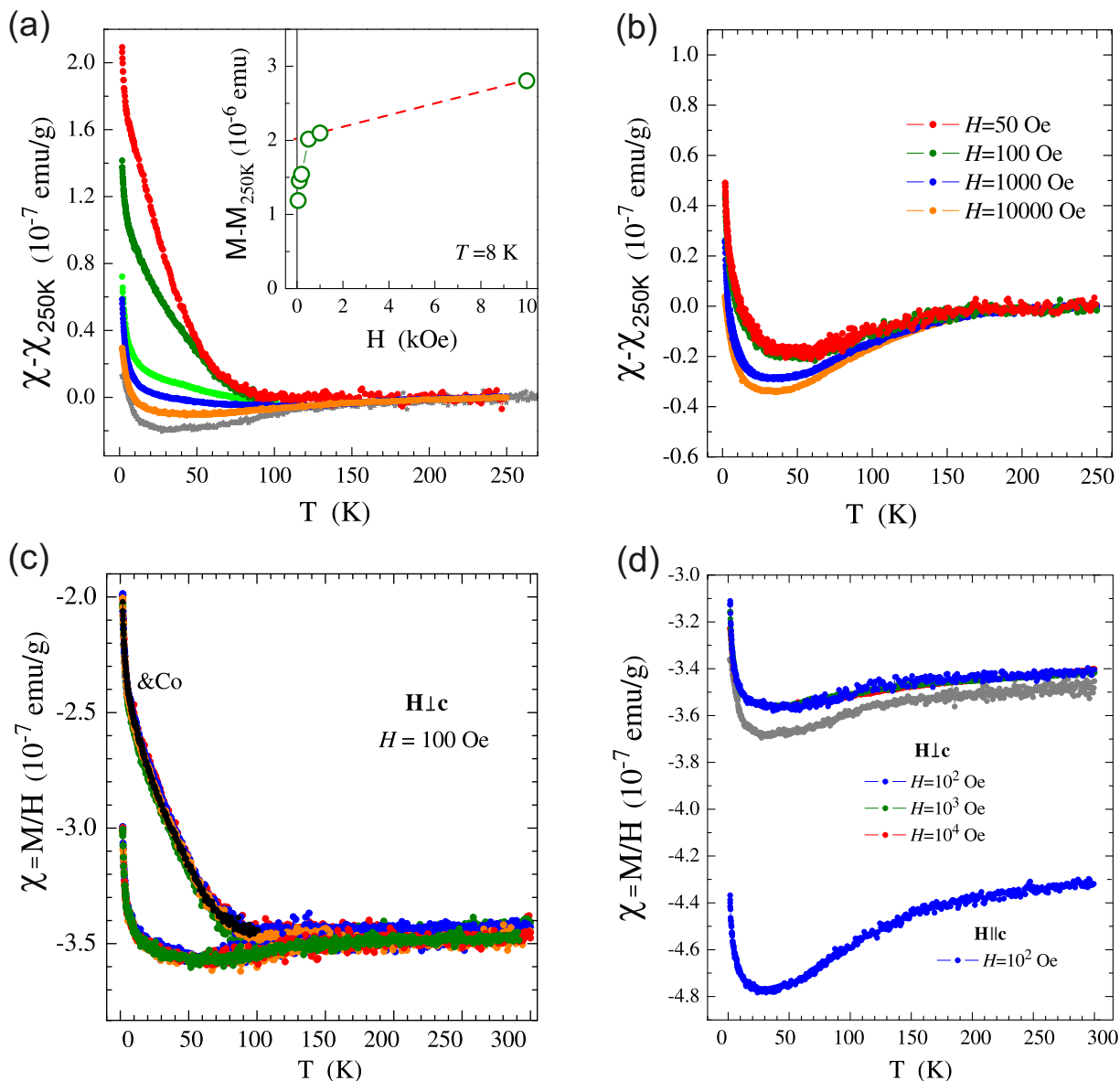
FIG. 5. (a) Temperature dependencies of the magnetic susceptibility for the in-plane magnetic field $H\perp c$, $H$=0.05 (red); 0.1 (olive); 0.5 (green); 1 (blue); 10 kOe (orange). Field-independent susceptibility data for the pristine BSTS2 surface are shown for comparison by gray dots. Insert shows $M(H)$ curve measured at $T$=8 K for $H\perp c$. (b) Temperature dependencies of the magnetic susceptibility for the out-of-plane magnetic field $H\parallel c$. (c) Magnetic susceptibility for $H\perp c$, $H$=0.1 kOe of a crystal before and after the removal of a cobalt-rich surface layer with duct tape (different colors show several heating-cooling runs). The data shown by black symbols were taken half a year earlier to check the surface-state stability. (d) Temperature dependence of the magnetic susceptibility for the crystal with a large amount of deposited Co [Fig. 3(d)]. For comparison, the field-independent susceptibility of the pristine surface at $H\perp c$ is demonstrated in gray.

the normal to the surface. It is known that the in-plane magnetization leads to a dispersion energy shift along the momentum vector perpendicular to the magnetization in the momentum space, while the presence of an out-of-plane component induces an energy gap in TIs. The in-plane magnetization is presumably isotropic within the plane and has almost zero remanence according to SQUID measurements, which accounts for the ARPES data demonstrating absence of any dispersion $k$ shift. In contrast, the absence of symmetry with respect to the surface normal can induce remanent magnetization in the Co-containing layer and, as a result, the appearance of a gap in TI surface states (Fig. 2). In order to confirm that the observed

unusual FM properties originate from the cobalt-rich surface layer of the crystal rather than the bulk, a thin top layer with cobalt was removed with duct tape. Figure 5(c) shows the magnetic susceptibility data of a crystal taken before and after the top-layer removal, which demonstrates unambiguously that the FM state belongs to the top crystal's layer.

The observed temperature range for the gap opening, which is in agreement with the temperature range, where out-of-plane magnetization is detected by SQUID, is far above typical Curie temperature of about 30 K, observed in the optimal Cr- or V-doped TIs [8,9,13,17]. However, it was demonstrated that bulk and subsurface impurities in TIs can

generate not only localized states in the gap [57–59] but also impurity-derived resonance bands, which can hybridize with the Dirac state [60,61]. In case of magnetic impurity with out-of-plane magnetization, irrespective the magnetic moments ordering, the hybridization of exchange-split resonance states with the Dirac state can facilitate the gap opening [61]. The essential role of impurity-state-mediated exchange interaction in the magnetic properties of V-doped and Cr-doped $(Bi, Sb)_2Te_3$ was also established in Ref. [62]. Thus, we can speculate that the spin-split resonant states can mediate the gap opening in our system with Co-doped surface up to the temperature at which out-of-plane magnetization is maintained.

The magnetic properties of a crystal with a large amount of deposited Co, when the mattagamite-type $CoTe_xSe_{2-x}$ structure completely covers the surface [corresponding to the Fig. 3(d)], were also studied by SQUID [Fig. 5(d)]. For this crystal, the magnetic susceptibility behavior is similar to that observed for initial Co-free crystal [gray curve in Fig. 5(d)] and no signs of FM response have been found. The change in magnetic behavior with the Co-layer thickness can be accounted for by the cobalt segregation into orthorhombic $CoTe_2$ and $CoSe_2$ compounds that are paramagnetic [63–65], while the measured FM contribution comes from Co atoms that substitute pnictogens in the original structure. According to our calculations Co atomic magnetic moments, being of $0.25\,\mu_B$ in parent $CoTe_2$ and $CoSe_2$, decrease in disordered CoTeSe solid solution, where an average Co magnetic moment is of $\sim0.16\,\mu_B$. However, the total energy of the paramagnetic phase is 2.2 meV lower comparing with the ferromagnetic calculation and hence the CoTeSe solid solution is a paramagnetlike parent $CoTe_2$ and $CoSe_2$. A situation when a 2D ferromagnetic phase became paramagnetic in the bulk is known from the literature. For example, it occurs in the $MnSe_2$:Se-Mn-Se monolayer, which being prepared on $SnSe_2$ or GaSe, exhibits a 2D ferromagnetism, while bulk $MnSe_2$ has a cubic pyrite or rocksalt structure with paramagnetic properties [66].

One can conclude from ARPES and SQUID measurements that there is a certain range of cobalt coverage 0.6–1.5 atoms/cell, which corresponds to partial replacement of pnictogen atoms with cobalt in the topmost QL of BSTS2 with the formation of ferromagnetic phase in this QL. In this case, the layer concentration of cobalt reaches 0.6 atoms/cell with respect to bismuth (antimony), which cannot be achieved by the crystal bulk doping. At lower coverage the exchange interaction is weak to induce a long-range

ferromagnetism and gap opening, while at higher coverages (above 3 atoms/cell) the solid solution becomes unstable and paramagnetic $CoTe_xSe_{2-x}$ is formed.

## IV. CONCLUSIONS

To summarize, our findings offer a versatile way to control the formation of magnetically doped topological insulator surfaces with sizable Dirac cone gaps, which are stable over a wide temperature range. This can be achieved by precise deposition of magnetic atoms at a temperature of $300°–330\,°C$. This finding is in a stark contrast with earlier works on magnetic metal atoms (Co, Ni, Fe) deposition on $Bi_2Se_3$ TI [36,51–53,67], where the deposition temperature was ranged as 15 K – RT, and no gap opening was observed. We found that deposition of Co or Mn atoms within 0.6–3 atom/cell effective thickness at elevated temperature results in substitution of pnictogene atoms in the BSTS2 surface layer with magnetic dopants leading to formation of a 2D magnetic phase with out-of-plane magnetization, which is stable up to $\approx100$ K as affirmed by our SQUID measurements. In contrast, the deposition of magnetic atoms at room temperature leads to progressive surface disordering proven by the degradation of the LEED pattern and ARPES spectrum. Along with the formation of a diluted magnetic surface layer with out-of-plane magnetization, islands of a paramagnetic $CoTe_xSe_{2-x}$ mattagamitelike phase are formed which—at 3 atoms/cell and larger deposition—cover a significant part of the BSTS2 surface, hindering the ARPES measurements of the topological surface states when coverage is more than 3 atoms/cell.

## ACKNOWLEDGMENTS

[1] M. Z. Hasan and C. L. Kane, Colloquium: Topological insulators, Rev. Mod. Phys. **82**, 3045 (2010).

[2] X.-L. Qi and S.-C. Zhang, Topological insulators and superconductors, Rev. Mod. Phys. **83**, 1057 (2011).

[3] X.-L. Qi, T. L. Hughes, and S.-C. Zhang, Topological field theory of time-reversal invariant insulators, Phys. Rev. B **78**, 195424 (2008).

[4] X.-L. Qi, T. L. Hughes, and S.-C. Zhang, Chiral topological superconductor from the quantum Hall state, Phys. Rev. B **82**, 184516 (2010).

[5] Q. L. He, L. Pan, A. L. Stern, E. C. Burks, X. Che, G. Yin, J. Wang, B. Lian, Q. Zhou, E. S. Choi, K. Murata, X. Kou, Z. Chen, T. Nie, Q. Shao, Y. Fan, S.-C. Zhang, K. Liu, J. Xia, and K. L. Wang, Chiral Majorana fermion modes in a quantum anomalous Hall insulator–superconductor structure, Science **357**, 294 (2017).

[6] M. M. Otrokov, I. I. Klimovskikh, H. Bentmann, D. Estyunin, A. Zeugner, Z. S. Aliev, S. Gaß, A. U. B. Wolter, A. V. Koroleva, A. M. Shikin, M. Blanco-Rey, M. Hoffmann, I. P. Rusinov, A. Y. Vyazovskaya, S. V. Eremeev, Y. M.

Koroteev, V. M. Kuznetsov, F. Freyse, J. Sánchez-Barriga, I. R. Amiraslanov *et al.*, Prediction and observation of an antiferromagnetic topological insulator, Nature (London) **576**, 416 (2019).

[7] Y. L. Chen, J.-H. Chu, J. G. Analytis, Z. K. Liu, K. Igarashi, H.-H. Kuo, X. L. Qi, S. K. Mo, R. G. Moore, D. H. Lu, M. Hashimoto, T. Sasagawa, S. C. Zhang, I. R. Fisher, Z. Hussain, and Z. X. Shen, Massive Dirac fermion on the surface of a magnetically doped topological insulator, Science **329**, 659 (2010).

[8] C.-Z. Chang, J. Zhang, X. Feng, J. Shen, Z. Zhang, M. Guo, K. Li, Y. Ou, P. Wei, L.-L. Wang, Z.-Q. Ji, Y. Feng, S. Ji, X. Chen, J. Jia, X. Dai, Z. Fang, S.-C. Zhang, K. He, Y. Wang *et al.*, Experimental observation of the quantum anomalous Hall effect in a magnetic topological insulator, Science **340**, 167 (2013).

[9] J. G. Checkelsky, R. Yoshimi, A. Tsukazaki, K. S. Takahashi, Y. Kozuka, J. Falson, M. Kawasaki, and Y. Tokura, Trajectory of the anomalous Hall effect towards the quantized state in a ferromagnetic topological insulator, Nat. Phys. **10**, 731 (2014).

[10] C.-Z. Chang, P. Tang, Y.-L. Wang, X. Feng, K. Li, Z. Zhang, Y. Wang, L.-L. Wang, X. Chen, C. Liu, W. Duan, K. He, X.-C. Ma, and Q.-K. Xue, Chemical-Potential-Dependent Gap Opening at the Dirac Surface States of Bi$_2$Se$_3$ Induced by Aggregated Substitutional Cr Atoms, Phys. Rev. Lett. **112**, 056801 (2014).

[11] X. Kou, S.-T. Guo, Y. Fan, L. Pan, M. Lang, Y. Jiang, Q. Shao, T. Nie, K. Murata, J. Tang, Y. Wang, L. He, T.-K. Lee, W.-L. Lee, and K. L. Wang, Scale-Invariant Quantum Anomalous Hall Effect in Magnetic Topological Insulators Beyond the Two-Dimensional Limit, Phys. Rev. Lett. **113**, 137201 (2014).

[12] A. Kandala, A. Richardella, S. Kempinger, C.-X. Liu, and N. Samarth, Giant anisotropic magnetoresistance in a quantum anomalous Hall insulator, Nat. Commun. **6**, 7434 (2015).

[13] X. Kou, L. Pan, J. Wang, Y. Fan, E. S. Choi, W.-L. Lee, T. Nie, K. Murata, Q. Shao, S.-C. Zhang, and K. L. Wang, Metal-to-insulator switching in quantum anomalous Hall states, Nat. Commun. **6**, 8474 (2015).

[14] Y. Feng, X. Feng, Y. Ou, J. Wang, C. Liu, L. Zhang, D. Zhao, G. Jiang, S.-C. Zhang, K. He, X. Ma, Q.-K. Xue, and Y. Wang, Observation of the Zero Hall Plateau in a Quantum Anomalous Hall Insulator, Phys. Rev. Lett. **115**, 126801 (2015).

[15] A. J. Bestwick, E. J. Fox, X. Kou, L. Pan, K. L. Wang, and D. Goldhaber-Gordon, Precise Quantization of the Anomalous Hall Effect Near Zero Magnetic Field, Phys. Rev. Lett. **114**, 187201 (2015).

[16] S. Grauer, S. Schreyeck, M. Winnerlein, K. Brunner, C. Gould, and L. W. Molenkamp, Coincidence of superparamagnetism and perfect quantization in the quantum anomalous Hall state, Phys. Rev. B **92**, 201304(R) (2015).

[17] C.-Z. Chang, W. Zhao, D. Y. Kim, H. Zhang, B. A. Assaf, D. Heiman, S.-C. Zhang, C. Liu, M. H. W. Chan, and J. S. Moodera, High-precision realization of robust quantum anomalous Hall state in a hard ferromagnetic topological insulator, Nat. Mater. **14**, 473 (2015).

[18] M. F. Islam, C. M. Canali, A. Pertsova, A. Balatsky, S. K. Mahatha, C. Carbone, A. Barla, K. A. Kokh, O. E. Tereshchenko, E. Jiménez, N. B. Brookes, P. Gargiani, M. Valvidares, S. Schatz, T. R. F. Peixoto, H. Bentmann, F. Reinert, J. Jung, T. Bathon, K. Fauth *et al.*, Systematics of electronic and magnetic properties in the transition metal doped Sb$_2$Te$_3$ quantum anomalous Hall platform, Phys. Rev. B **97**, 155429 (2018).

[19] D. Zhang, A. Richardella, D. W. Rench, S.-Y. Xu, A. Kandala, T. C. Flanagan, H. Beidenkopf, A. L. Yeats, B. B. Buckley, P. V. Klimov, D. D. Awschalom, A. Yazdani, P. Schiffer, M. Z. Hasan, and N. Samarth, Interplay between ferromagnetism, surface states, and quantum corrections in a magnetically doped topological insulator, Phys. Rev. B **86**, 205127 (2012).

[20] Y. S. Hor, P. Roushan, H. Beidenkopf, J. Seo, D. Qu, J. G. Checkelsky, L. A. Wray, D. Hsieh, Y. Xia, S.-Y. Xu, D. Qian, M. Z. Hasan, N. P. Ong, A. Yazdani, and R. J. Cava, Development of ferromagnetism in the doped topological insulator Bi$_{2-x}$Mn$_x$Te$_3$, Phys. Rev. B **81**, 195203 (2010).

[21] H. J. von Bardeleben, J. L. Cantin, D. M. Zhang, A. Richardella, D. W. Rench, N. Samarth, and J. A. Borchers, Ferromagnetism in Bi$_2$Se$_3$:Mn epitaxial layers, Phys. Rev. B **88**, 075149 (2013).

[22] R. Tarasenko, M. Vališka, M. Vondráček, K. Horáková, V. Tkáč, K. Carva, P. Baláž, V. Holý, G. Springholz, V. Sechovský, and J. Honolka, Magnetic and structural properties of Mn-doped Bi$_2$Se$_3$ topological insulators, Phys. B: Condens. Matter **481**, 262 (2016).

[23] J. Henk, M. Flieger, I. V. Maznichenko, I. Mertig, A. Ernst, S. V. Eremeev, and E. V. Chulkov, Topological Character and Magnetism of the Dirac State in Mn-Doped Bi$_2$Te$_3$, Phys. Rev. Lett. **109**, 076801 (2012).

[24] K. Carva, J. Kudrnovský, F. Máca, V. Drchal, I. Turek, P. Baláž, V. Tkáč, V. Holý, V. Sechovský, and J. Honolka, Electronic and transport properties of the Mn-doped topological insulator Bi$_2$Te$_3$: A first-principles study, Phys. Rev. B **93**, 214409 (2016).

[25] J. Henk, A. Ernst, S. V. Eremeev, E. V. Chulkov, I. V. Maznichenko, and I. Mertig, Complex Spin Texture in the Pure and Mn-Doped Topological Insulator Bi$_2$Te$_3$, Phys. Rev. Lett. **108**, 206801 (2012).

[26] J. A. Hagmann, X. Li, S. Chowdhury, S.-N. Dong, S. Rouvimov, S. J. Pookpanratana, K. Man Yu, T. A. Orlova, T. B. Bolin, C. U. Segre, D. G. Seiler, C. A. Richter, X. Liu, M. Dobrowolska, and J. K. Furdyna, Molecular beam epitaxy growth and structure of self-assembled Bi$_2$Se$_3$/Bi$_2$MnSe$_4$ multilayer heterostructures, New J. Phys. **19**, 085002 (2017).

[27] E. D. L. Rienks, S. Wimmer, J. Sánchez-Barriga, O. Caha, P. S. Mandal, J. Ruzicka, A. Ney, H. Steiner, V. V. Volobuev, H. Groiss, M. Albu, G. Kothleitner, J. Michalicka, S. A. Khan, J. Minár, H. Ebert, G. Bauer, F. Freyse, A. Varykhalov, O. Rader *et al.*, Large magnetic gap at the Dirac point in Bi$_2$Te$_3$/MnBi$_2$Te$_4$ heterostructures, Nature (London) **576**, 423 (2019).

[28] R. Lu, H. Sun, S. Kumar, Y. Wang, M. Gu, M. Zeng, Y.-J. Hao, J. Li, J. Shao, X.-M. Ma, Z. Hao, K. Zhang, W. Mansuer, J. Mei, Y. Zhao, C. Liu, K. Deng, W. Huang, B. Shen, K. Shimada *et al.*, Half-Magnetic Topological Insulator with Magnetization-Induced Dirac Gap at a Selected Surface, Phys. Rev. X **11**, 011039 (2021).

[29] T. Hirahara, S. V. Eremeev, T. Shirasawa, Y. Okuyama, T. Kubo, R. Nakanishi, R. Akiyama, A. Takayama, T. Hajiri, S.-i. Ideta, M. Matsunami, K. Sumida, K. Miyamoto, Y. Takagi, K. Tanaka, T. Okuda, T. Yokoyama, S.-i. Kimura, S. Hasegawa, and E. V. Chulkov, Large-gap magnetic topological heterostructure formed by subsurface incorporation of a ferromagnetic layer, Nano Lett. **17**, 3493 (2017).

[30] M. M. Otrokov, T. V. Menshchikova, M. G. Vergniory, I. P. Rusinov, A. Yu Vyazovskaya, Y. M. Koroteev, G. Bihlmayer,

A. Ernst, P. M. Echenique, A. Arnau, and E. V. Chulkov, Highly-ordered wide bandgap materials for quantized anomalous Hall and magnetoelectric effects, 2D Mater. **4**, 025082 (2017).

[31] S. V. Eremeev, M. M. Otrokov, and E. V. Chulkov, New universal type of interface in the magnetic insulator/topological insulator heterostructures, Nano Lett. **18**, 6521 (2018).

[32] T. Hirahara, M. M. Otrokov, T. T. Sasaki, K. Sumida, Y. Tomohiro, S. Kusaka, Y. Okuyama, S. Ichinokura, M. Kobayashi, Y. Takeda, K. Amemiya, T. Shirasawa, S. Ideta, K. Miyamoto, K. Tanaka, S. Kuroda, T. Okuda, K. Hono, S. V. Eremeev, and E. V. Chulkov, Fabrication of a novel magnetic topological heterostructure and temperature evolution of its massive Dirac cone, Nat. Commun. **11**, 4821 (2020).

[33] L. A. Wray, S.-Y. Xu, Y. Xia, D. Hsieh, A. V. Fedorov, Y. S. Hor, R. J. Cava, A. Bansil, H. Lin, and M. Z. Hasan, A topological insulator surface under strong Coulomb, magnetic and disorder perturbations, Nat. Phys. **7**, 32 (2011).

[34] L. R. Shelford, T. Hesjedal, L. Collins-McIntyre, S. S. Dhesi, F. Maccherozzi, and G. van der Laan, Electronic structure of Fe and Co magnetic adatoms on $Bi_2Te_3$ surfaces, Phys. Rev. B **86**, 081304(R) (2012).

[35] J. Honolka, A. A. Khajetoorians, V. Sessi, T. O. Wehling, S. Stepanow, J.-L. Mi, B. B. Iversen, T. Schlenk, J. Wiebe, N. B. Brookes, A. I. Lichtenstein, P. Hofmann, K. Kern, and R. Wiesendanger, In-Plane Magnetic Anisotropy of Fe Atoms on $Bi_2Se_3$(111), Phys. Rev. Lett. **108**, 256811 (2012).

[36] M. Ye, S. V. Eremeev, K. Kuroda, E. E. Krasovskii, E. V. Chulkov, Y. Takeda, Y. Saitoh, K. Okamoto, S. Y. Zhu, K. Miyamoto, M. Arita, M. Nakatake, T. Okuda, Y. Ueda, K. Shimada, H. Namatame, M. Taniguchi, and A. Kimura, Quasiparticle interference on the surface of $Bi_2Se_3$ induced by cobalt adatom in the absence of ferromagnetic ordering, Phys. Rev. B **85**, 205317 (2012).

[37] D. West, Y. Y. Sun, S. B. Zhang, T. Zhang, X. Ma, P. Cheng, Y. Y. Zhang, X. Chen, J. F. Jia, and Q. K. Xue, Identification of magnetic dopants on the surfaces of topological insulators: Experiment and theory for Fe on $Bi_2Te_3$(111), Phys. Rev. B **85**, 081305(R) (2012).

[38] A. Polyakov, H. L. Meyerheim, E. D. Crozier, R. A. Gordon, K. Mohseni, S. Roy, A. Ernst, M. G. Vergniory, X. Zubizarreta, M. M. Otrokov, E. V. Chulkov, and J. Kirschner, Surface alloying and iron selenide formation in $Fe/Bi_2Se_3$(0001) observed by x-ray absorption fine structure experiments, Phys. Rev. B **92**, 045423 (2015).

[39] J. Sánchez-Barriga, A. Varykhalov, G. Springholz, H. Steiner, R. Kirchschlager, G. Bauer, O. Caha, E. Schierle, E. Weschke, A. A. Ünal, S. Valencia, M. Dunst, J. Braun, H. Ebert, J. Minár, E. Golias, L. V. Yashina, A. Ney, V. Holý, and O. Rader, Nonmagnetic band gap at the Dirac point of the magnetic topological insulator $(Bi_{1-x}Mn_x)_2Se_3$, Nat. Commun. **7**, 10559 (2016).

[40] E. Golias, E. Weschke, T. Flanagan, E. Schierle, A. Richardella, E. D. L. Rienks, P. S. Mandal, A. Varykhalov, J. Sánchez-Barriga, F. Radu, N. Samarth, and O. Rader, Magnetization relaxation and search for the magnetic gap in bulk-insulating V-doped $(Bi, Sb)_2Te_3$, Appl. Phys. Lett. **119**, 132404 (2021).

[41] Y. Xu, I. Miotkowski, C. Liu, J. Tian, H. Nam, N. Alidoust, J. Hu, C.-K. Shih, M. Z. Hasan, and Y. P. Chen, Observation of topological surface state quantum Hall effect in an intrinsic three-dimensional topological insulator, Nat. Phys. **10**, 956 (2014).

[42] A. Sulaev, M. Zeng, S.-Q. Shen, S. K. Cho, W. G. Zhu, Y. P. Feng, S. V. Eremeev, Y. Kawazoe, L. Shen, and L. Wang, Electrically tunable in-plane anisotropic magnetoresistance in topological insulator $BiSbTeSe_2$ nanodevices, Nano Lett. **15**, 2061 (2015).

[43] G. Kresse and J. Hafner, *Ab initio* molecular dynamics for liquid metals, Phys. Rev. B **47**, 558 (1993).

[44] G. Kresse and J. Furthmüller, Efficient iterative schemes for *ab initio* total-energy calculations using a plane-wave basis set, Phys. Rev. B **54**, 11169 (1996).

[45] P. E. Blöchl, Projector augmented-wave method, Phys. Rev. B **50**, 17953 (1994).

[46] G. Kresse and D. Joubert, From ultrasoft pseudopotentials to the projector augmented-wave method, Phys. Rev. B **59**, 1758 (1999).

[47] J. P. Perdew, K. Burke, and M. Ernzerhof, Generalized Gradient Approximation Made Simple, Phys. Rev. Lett. **77**, 3865 (1996).

[48] S. Grimme, S. Ehrlich, and L. Goerigk, Effect of the damping function in dispersion corrected density functional theory, J. Comput. Chem. **32**, 1456 (2011).

[49] A. Zunger, S.-H. Wei, L. G. Ferreira, and J. E. Bernard, Special Quasirandom Structures, Phys. Rev. Lett. **65**, 353 (1990).

[50] K. Okhotnikov, T. Charpentier, and S. Cadars, Supercell program: a combinatorial structure-generation approach for the local-level modeling of atomic substitutions and partial occupancies in crystals, Journal of Cheminformatics **8**, 17 (2016).

[51] M. R. Scholz, J. Sánchez-Barriga, D. Marchenko, A. Varykhalov, A. Volykhov, L. V. Yashina, and O. Rader, Tolerance of Topological Surface States Towards Magnetic Moments: Fe on $Bi_2Se_3$, Phys. Rev. Lett. **108**, 256810 (2012).

[52] M. Scholz, M. Sanchez-Barriga, D. Marchenko, A. Varykhalov, A. Volykhov, L. Yashina, and O. Rader, Intact Dirac cone of $Bi_2Te_3$ covered with a monolayer Fe, Physica Status Solidi RRL **7(1-2)**, 139 (2013).

[53] T. Valla, Z.-H. Pan, D. Gardner, Y. S. Lee, and S. Chu, Photoemission Spectroscopy of Magnetic and Nonmagnetic Impurities on the Surface of the $Bi_2Se_3$ Topological Insulator, Phys. Rev. Lett. **108**, 117601 (2012).

[54] See Supplemental Material at http://link.aps.org/supplemental/10.1103/PhysRevMaterials.5.124204 for ARPES study of the Co-deposited BSTS2 at different temperatures and for band-gap opening in the BSTS2 caused by the sub-angstrom Mn deposition.

[55] S. M. Suturin, A. M. Korovin, V. V. Fedorov, G. A. Valkovsky, M. Tabuchi, and N. S. Sokolov, An advanced three-dimensional RHEED mapping approach to the diffraction study of $Co/MnF_2/CaF_2/Si$(001) epitaxial heterostructures, J. Appl. Crystallogr. **49**, 1532 (2016).

[56] R. P. Gupta, O. D. Iyore, K. Xiong, J. B. White, K. Cho, H. N. Alshareef, and B. E. Gnade, Interface characterization of cobalt contacts on bismuth selenium telluride for thermoelectric devices, Electrochem. Solid-State Lett. **12**, H395 (2009).

[57] R. R. Biswas and A. V. Balatsky, Impurity-induced states on the surface of three-dimensional topological insulators, Phys. Rev. B **81**, 233405 (2010).

[58] A. M. Black-Schaffer and A. V. Balatsky, Strong potential impurities on the surface of a topological insulator, Phys. Rev. B **85**, 121103(R) (2012).

[59] A. M. Black-Schaffer and A. V. Balatsky, Subsurface impurities and vacancies in a three-dimensional topological insulator, Phys. Rev. B **86**, 115433 (2012).

[60] L. Miao, Y. Xu, W. Zhang, D. Older, S. A. Breitweiser, E. Kotta, H. He, T. Suzuki, J. D. Denlinger, R. R. Biswas, J. G. Checkelsky, W. Wu, and L. A. Wray, Observation of a topological insulator Dirac cone reshaped by nonmagnetic impurity resonance, npj Quantum Mater. **3**, 29 (2018).

[61] Y. Xu, J. Chiu, L. Miao, H. He, Z. Alpichshev, A. Kapitulnik, R. R. Biswas, and L. A. Wray, Disorder enabled band structure engineering of a topological insulator surface, Nat. Commun. **8**, 14081 (2017).

[62] T. R. F. Peixoto, H. Bentmann, P. Rüßmann, A.-V. Tcakaev, M. Winnerlein, S. Schreyeck, S. Schatz, R. C. Vidal, F. Stier, V. Zabolotnyy, R. J. Green, C. H. Min, C. I. Fornari, H. Maaß, H. B. Vasili, P. Gargiani, M. Valvidares, A. Barla, J. Buck, M. Hoesch *et al.*, Non-local effect of impurity states on the ex-

change coupling mechanism in magnetic topological insulators, npj Quantum Mater. **5**, 87 (2020).

[63] R. Shi, X. Liu, Y. Shi, R. Ma, B. Jia, H. Zhang, and G. Qui, Selective synthesis and magnetic properties of uniform CoTe and CoTe$_2$ nanotubes, J. Mater. Chem. **20**, 7634 (2010).

[64] K. Persson, Materials Data on CoTe$_2$ (SG:58) by Materials Project (2016).

[65] K. Persson, Materials Data on CoSe$_2$ (SG:58) by Materials Project (2015).

[66] D. O'Hara, T. Zhu, A. Trout, A. Ahmed, Y. Luo, C. Lee, M. Brenner, S. Rajah, J. Gupta, D. McComb, and R. Kawakami, Room temperature intrinsic ferromagnetism in epitaxial manganese selenide films in the monolayer limit, Nano Lett. **18**, 3125 (2018).

[67] I. Vobornik, G. Panaccione, J. Fujii, Z.-H. Zhu, F. Offi, B. Salles, F. Borgatti, P. Torelli, J. Rueff, D. Ceolin, A. Artioli, M. Unnikrishnan, G. Levy, M. Marangolo, M. Eddrief, D. Krizmancic, H. Ji, A. Damascelli, G. van der Laan, R. Egdell *et al.*, Observation of distinct bulk and surface chemical environments in a topological insulator under magnetic doping, J. Phys. Chem. C **118**, 12333 (2014).